Received: 7 March 2017 | Revised: 19 May 2017 | Accepted: 22 May 2017

DOI: 10.1002/ppap.201700052

FULL PAPER

PLASMA PROCESSES AND POLYMERS

Porous zinc oxide nanocrystalline film deposition by atmospheric pressure plasma: Fabrication and energy band estimation

Gunisha Jain | **Manuel Macias-Montero** | **Tamilselvan Velusamy** | **Paul Maguire** | **Davide Mariotti**

Nanotechnology and Integrated Bioengineering Centre, Ulster University, Newtownabbey, UK

Correspondence
Gunisha Jain, Nanotechnology and Integrated Bioengineering Centre, Ulster University, Shore Road, Newtownabbey BT37 0QB, UK.
Email: jain-G@email.ulster.ac.uk

Funding information
Engineering and Physical Sciences Research Council, Grant number: EP/M024938/1 and EP/K022237/1

Porous ZnO nanocrystalline films have drawn research attention due to improvement in gas sensing, adsorption, photocatalytic, and photovoltaic applications. However, scalable synthesis of porous nanostructures has been a challenge. Here, This paper reports a very easy, fast, and scalable one-step process for synthesis and deposition of porous ZnO nanocrystalline film by low-temperature atmospheric pressure plasma. The plasma is generated with radio frequency power using a metallic zinc wire as a precursor. Nanostructures have been synthesized and agglomerate to form a porous film at the substrate. Energy band structure of the deposited film has been investigated to understand the corresponding band alignment, which is relevant to many applications. An in-depth study of the grown nanostructured ZnO film has been included and characterized by X-ray diffraction, transmission electron microscopy, X-ray photoelectron spectroscopy, kelvin probe measurement, ultra-violet/visible absorption, and photoluminescence.

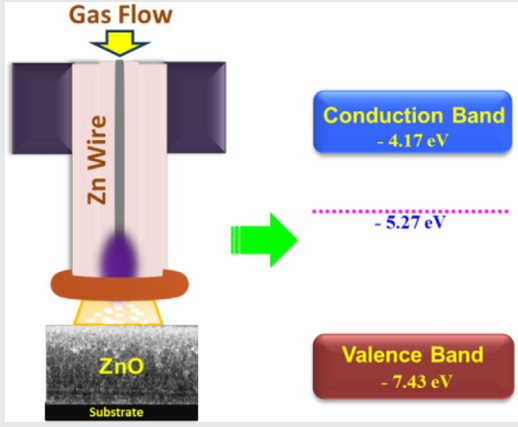

KEYWORDS
band estimation, kelvin probe measurement, nanocrystalline films, non-thermal plasma, Raman spectroscopy

1 | INTRODUCTION

Zinc oxide (ZnO) is a material of great interest that is widely used in a large variety of applications such as ultra-violet (UV) absorber, as a transparent and conductive layer in photovoltaic devices, as a piezoelectric material, and in other optoelectronic applications including light-emitting diodes.[1–10] ZnO has a wide bandgap (~3.3 eV) with a large

exciton binding energy (~60 meV) and high electron mobility.[11] The n-type conducting nature with the wide bandgap, non-toxicity, and good optical transmittance makes it highly suitable for instance as an electron acceptor or transparent electrode in solar cells.

Interest in developing porous ZnO nanocrystalline film has increased because of its high surface area,[12] increased photocatalytic activity,[13] and long-range charge transport.[14] Here we will show porous ZnO nanocrystalline film synthesis by radio-frequency (RF) atmospheric pressure plasma (APP) using environmental oxygen. Previously studied methods for compact ZnO film synthesis includes molecular beam epitaxy,[15,16] MOCVD,[17–20] sol-gel process,[21–24] and spray pyrolysis.[25–30] Most of these techniques require complex vacuum-based systems or operate with a low yield. Other processes that use wet chemistry are also generally slow and produce undesirable reaction by-products, which can affect the film purity and lengthen the synthesis with required purification steps. However, very few techniques have been demonstrated for porous ZnO film deposition which mainly includes chemical synthesis.[31–34]

APPs have gained attention due to low-cost, process flexibility and the potential of scale-up. Only a few reports have demonstrated ZnO film deposition by APP. Chang et al. reported the deposition of In-doped ZnO films by an APP jet.[35] Recently Hsu et al. have deposited ZnO film with different salt precursors and studied the resulting film quality, which indicated zinc chloride to be the best-suited precursor for their process.[36] However, the use of salts as precursors may affect the purity of the film[37] and therefore the use of pure solid precursors can be highly advantageous both for improving the purity and reducing associated costs. Stauss et al. have used metallic zinc wire as a precursor with ultra-high frequency (UHF, 450 MHz) source to produce an inductively coupled plasma.[38] However, there is no report on porous ZnO nanocrystalline film deposition by APP.

Here, we will demonstrate direct deposition of porous ZnO nanocrystalline film directly consuming a metallic zinc wire as a precursor, oxidized by environmental oxygen. We further demonstrate that, at these conditions, the plasma produces nanocrystallites which are then assembled on the substrate to form a porous film.

2 | EXPERIMENTAL SECTION

The plasma system consisted of a stainless steel tube with quartz capillary (1 mm outer diameter and 0.7 mm internal diameter) containing a 99.99% pure zinc wire (Purchased from Alfa Aesar, Heysham, UK) of 0.25 mm diameter and a copper power electrode as shown in Figure 1a. The zinc wire acted as a ground electrode and radio frequency (RF) power (MKS Elite 300, 13.56 MHz) at 40 W is applied to the copper electrode via a matching unit; 150 standard cubic centimetre per minute (sccm) helium gas flow rate was used. We have investigated different processing parameters to identify these optimum conditions, at which highly uniform and reproducible film can be synthesized. The matching unit was between the electrode and the power supply, to reduce reflected power loss and to ensure plasma stability. The plasma was generated between the powered electrode and the zinc wire as shown in Figure 1a and b. The distance between the capillary and the substrate was 1.5 cm. The wire was consumed fairly quickly, about 1 cm in 10–20 s. It allows the deposition of the corresponding films on various substrates, including temperature-sensitive ones. This process is highly repeatable and capable of depositing uniform films reproducibly. However, a potential commercial deployment of this set-up will require engineering the precursor supply for prolonged deposition periods so to continuously feed the metal wire.

Furthermore, because the system was operating at atmospheric pressure, we were able to collect nanocrystallites in colloids by replacing the substrate with a vial containing ethanol.

This, in particular, confirmed that nanocrystallites were produced prior to deposition and that film formation was not due to radicals or ions but rather due to the agglomeration of

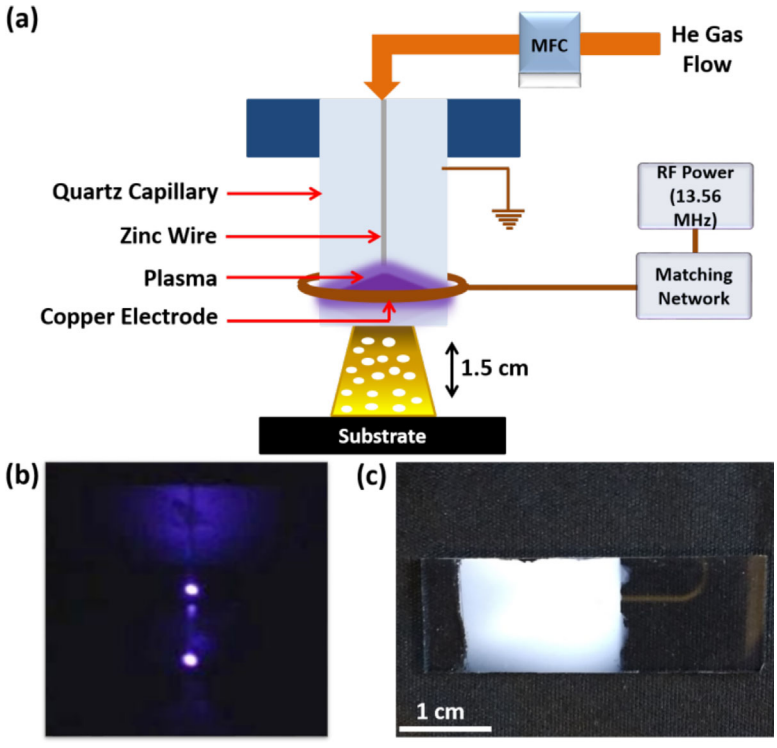

FIGURE 1 (a) Schematic of the synthesis set-up. (b) Photo of the plasma in operation. (c) Deposited ZnO film (white region) on indium-tin oxide-coated glass substrate

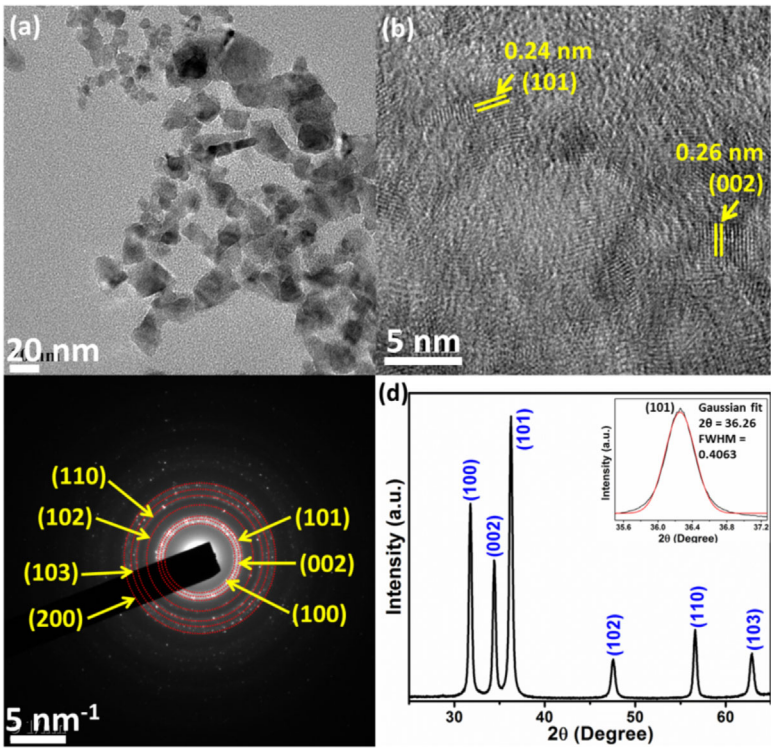

FIGURE 2 (a) Transmission electron microscope (TEM) image and (b) high-resolution TEM image of ZnO nanocrystallites. (c) Selective-area electron diffraction of the ZnO samples. (d) X-ray diffraction pattern of ZnO film and inset Scherrer particle size calculation

various nanoscale crystals. The deposited ZnO film on indium-tin oxide (ITO) coated glass substrate can be seen in Figure 1c.

The film was deposited on a glass substrate to identify the crystalline structure by X-ray diffraction (XRD; Bruker X8, Billerica, MA, USA). High-resolution transmission electron microscopy (HRTEM; Jeol JEM02100 F) was performed by collecting the sample in ethanol and drop-casting on carbon coated gold grids. Elemental analysis was carried out by energy-dispersive x-ray spectroscopy (EDX) attached to the TEM. The ZnO film was deposited on a silicon substrate to identify the nature of the chemical bonds by Fourier transform infrared spectroscopy (FTIR, Thermoscientific iS5, USA). The surface morphology was characterized in plain view and cross section using scanning electron microscopy (SEM; FEI Quanta 200 3D, Hillsboro, OR, USA). The X-ray photoelectron spectrum (XPS) was recorded to identify the chemical composition on X-ray spectrometer using Al K_α radiation. XPS measurements were also used to determine the valence band edge. Raman spectroscopy was performed by depositing the film on a molybdenum foil to exclude any interference from the background. He-Ne laser (632.8 nm) had been used for Raman analysis. The sample was deposited on ITO-conducting surface to carry out Kelvin probe (SKP 4.5, KP Technology Ltd., Wick, Caithness, Scotland) measurements, to find out Fermi level of the film. Finally, we measured optical characteristics using ultra-violet/visible (UV-Vis PerkinElmer LAMDA 365, Waltham, MA, USA) spectroscopy by collecting ZnO directly in ethanol and calculated the corresponding bandgap by Tauc plot. ZnO colloidal solution in ethanol was used to measure the photoluminescence (Cary eclipse fluorescence spectrophotometer, Agilent Tech., Santa Clara, CA, USA).

3 | RESULTS AND DISCUSSION

HRTEM micrograph and selective area electron diffraction (SAED) pattern of the colloidal sample are shown in Figure 2a–c. Figure 2a shows larger particles as well as small crystallites. The lattice images of particles were clearly observed in HRTEM as shown in Figure 2b. The interplanar spacing was calculated and found to be 0.24 nm and 0.26 nm which correspond to (101) and (002) planes of wurtzite ZnO, respectively. ZnO planes can be also observed in the SAED pattern in Figure 2c.

The SAED pattern consists of series of dotted rings which confirmed the polycrystalline nature and wurtzite structure of synthesised ZnO nanoparticles. The nature of material and purity was further verified by XRD analysis of the ZnO film on a glass substrate, as shown in Figure 2d.

As shown in Figure 2d, the film shows a crystalline nature. The peaks at 31.7°, 34.4°, 36.2°, 47.5°, 56.6°, and 62.8° correspond to the (100), (002), (101), (102), (110), and (103) planes of wurtzite zinc oxide, respectively.[39] XRD measurement also show the orientation of the planes, that is, a strong orientation along [101] direction as well as [100]. The average grain size was first calculated using Scherrer equation,

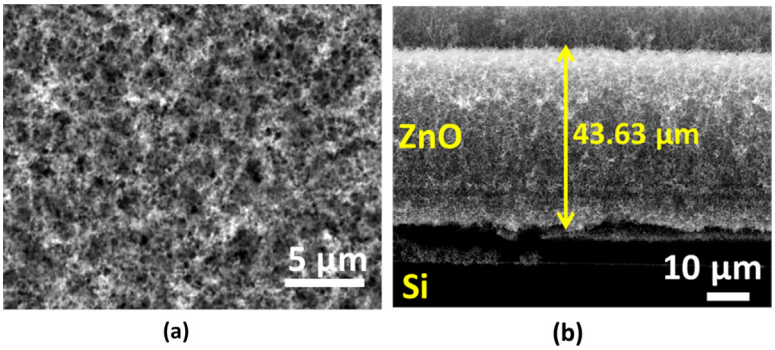

FIGURE 3 Scanning electron microscope image (a) Porous zinc oxide film grown on Si substrate (b) Cross section of the deposited film

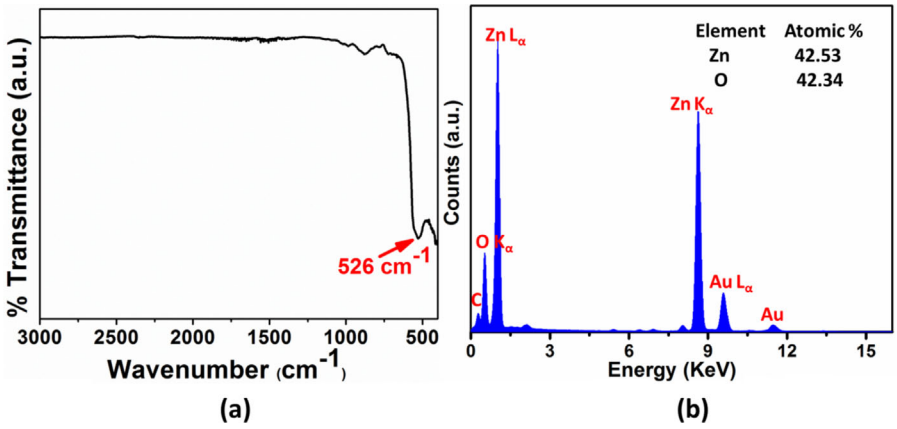

FIGURE 4 (a) Fourier transform infrared spectrum of prepared ZnO film. (b) Energy-dispersive X-ray analysis of ZnO

$$D = 0.9\lambda/\beta \cos\theta \quad (1)$$

where D is the grain size, λ is the X-ray wavelength (0.154 nm for Cu K_α), β is full-width at half maximum in radian for the diffraction peak (101) (inset Figure 2d) and θ is the Bragg angle. The average crystallite size (D) of ZnO was found to be 20.58 nm. Both TEM and XRD confirm the nanocrystalline nature of the film.

The surface morphology of the film deposited on a substrate was then analyzed by SEM as shown in Figure 3a. The porous nature of the film can be seen in the SEM image, which shows a high degree of uniformity. High porosity can be also observed in the cross section SEM image, shown in Figure 3b. This can be very useful in dye sensitized solar cell, in gas sensing application and in many other applications also.[40–42] The measured thickness of the film is 43.63 µm which was deposited under static conditions covering an area of 2.125 cm^2 in 10 s. Because of the high deposition rate of 4.363 µm/s, this technique can be very useful for bulk deposition of ZnO porous film in a single step.

The chemical composition of the film was analysed by FTIR, EDX, and XPS. The FTIR of ZnO shows stretching vibrations at 436–529 cm^{-1}.[43–46] In particular, a peak at 526 cm^{-1} can be observed in Figure 4a, which correspond to ZnO. No other peak could be observed in the FTIR spectrum. EDX performed on the colloidal sample also confirms ZnO composition. The presence of Zn and O and the atomic percentage of the individual element can be seen in Figure 4b. The peaks of gold and carbon are originating from the TEM grid.

Raman scattering spectroscopy was carried out to study the vibrational properties of porous ZnO. Raman spectrum was recorded at room temperature in the range of 250–650 cm^{-1} as shown in Figure 5. Only one vibrational peak was observed at 432 cm^{-1} which can be assigned to a fundamental optical E2 (high) mode.[47,48] This Raman peak of a ZnO crystal is the band characteristics of hexagonal wurtzite phase. Other phonon or multiple scattering peaks were absent in our measurement. A usually reported peak at 580 cm^{-1} related to intrinsic defects, such as an oxygen vacancy and interstitial zinc also did not appear suggesting good quality and stoichiometric ZnO as confirmed by EDX (see% composition in Figure 4b).[47]

XPS was performed to analyse further the chemical composition and oxidation states. The binding energy (BE) was calibrated against the C 1s (284.6 eV) as a reference. XPS survey shows Zn and O peaks as shown in Figure 6a and confirms ZnO formation. Binding energy at 1021.5 and 1044.6 eV are attributed to the binding energy of $Zn_{2p3/2}$ and $Zn_{2p1/2}$ electrons as shown in Figure 6b. The BE difference between these two peaks is 23.1 eV which suggest that Zn is in Zn^{+2} state, confirming ZnO formation.[49–51]

In the XPS spectra, the asymmetric O 1s peak was observed with a shoulder at higher binding energy. O 1s spectrum was fitted into three peaks centred at 530.12, 531.49, and 532.37 eV, Figure 6c. The first peak at 530.12 eV corresponds to O^{-2} in Zn-O binding. The peak at 531.49 eV correlates to the oxygen-deficient region in ZnO matrix or

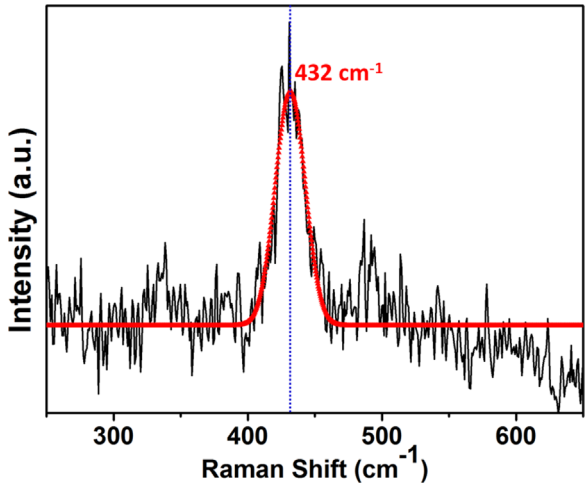

FIGURE 5 A typical Raman spectrum at room temperature of porous ZnO film

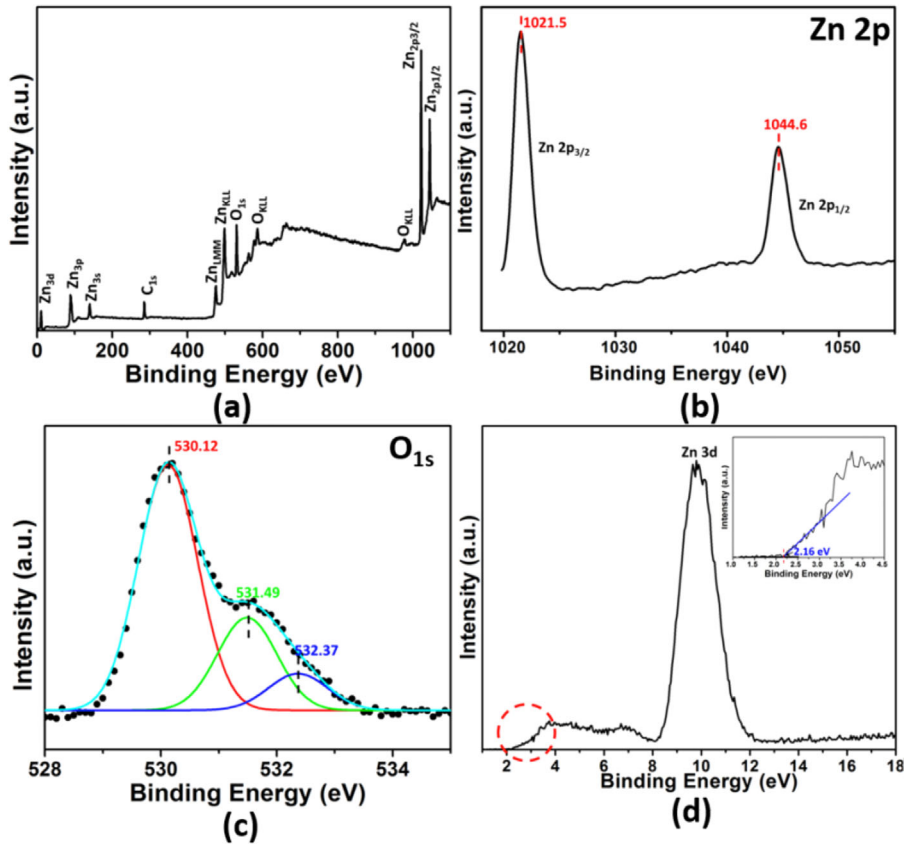

FIGURE 6 (a) X-ray photoelectron spectrum (XPS) survey scan of ZnO; (b) Zn 2p; (c) O 1 s; (d) onset of the XPS spectra of ZnO and inset shows E_f -E_{VBM}

O-H group absorbed on ZnO surface. Higher energy peak at 532.37 eV can be attributed to chemisorbed oxygen such as H_2O or $-CO_3$ species.[52,53]

The difference between Fermi level energy (E_f) and valence band maximum (E_{VBM}) was evaluated from the XPS spectra shown in Figure 6d. This was done by extrapolating the leading edge of the XPS spectra to the baseline as shown in the inset of Figure 6d. This produced a value of $(E_f - E_{VBM}) = 2.16$ eV.

In order to characterize the bandgap of the ZnO, we have carried out UV-Vis absorption spectroscopy. The result of this technique shows a strong excitonic absorption peak at 362 nm (Figure 7), which is close to the excitonic peak observed for bulk ZnO.[39,54]

ZnO is expected to have a direct bandgap and assuming scattering to be negligible in our measurements, we can use absorbance to determine the bandgap value through a Tauc plot (inset of Figure 7). This is done by plotting $(Ah\nu)^2$ versus $h\nu$ where A is the absorbance and $h\nu$ is the photon energy. The Tauc plot is shown in the inset of Figure 7. The direct bandgap is confirmed by the linear region of the plot and the intercept produces a bandgap of 3.26 eV.

ZnO generally shows photoluminescence in the UV and visible region. Ultra-violet emission corresponds to the bandgap excitonic emission and the visible emission is due to defects. In particular, visible emission could be due to recombination of the conduction band electron with deep-trap holes or recombination of electron present in near conduction band traps with holes in the valence band.[55]

We have recorded excitation and emission spectra of ZnO. Excitation spectra at emission wavelength 378 nm is measured which shows peaks at two excitation wavelengths, 275 nm and 338 nm (Figure 8 spectra (a)). We have observed

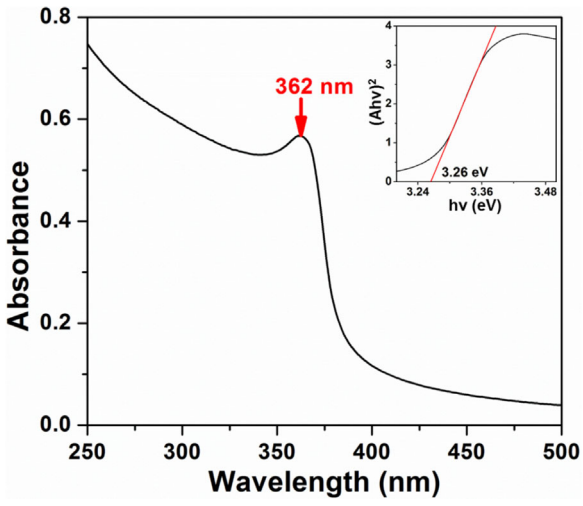

FIGURE 7 Ultra-violet/visible spectrum of ZnO and (inset) corresponding Tauc plot

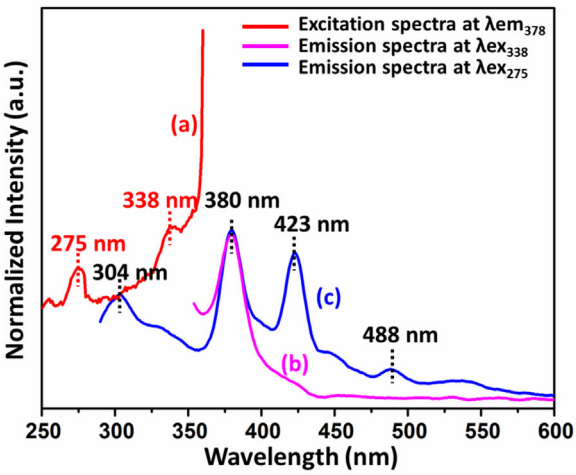

FIGURE 8 Photoluminescence spectra of ZnO shows a) Excitation spectra at λem_{378} b) high-intensity excitonic peak at λex_{338} and c) violet-blue emission as well with the excitonic peak at lower wavelength (λex_{275})

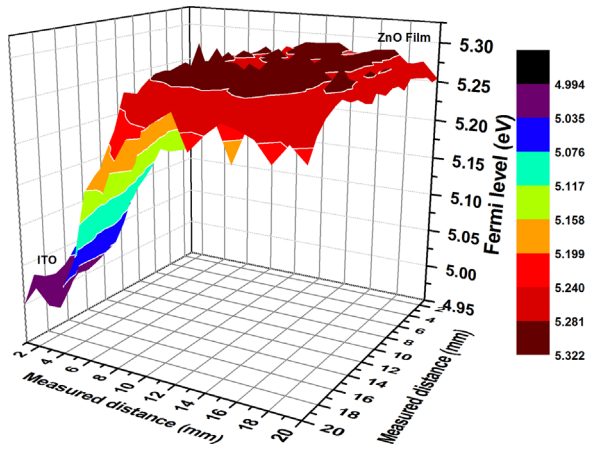

FIGURE 9 Fermi level measurement of ZnO film by scanning Kelvin probe on ITO substrate

PL with these two different excitation wavelengths of 338 nm and 275 nm shown in Figure 8 spectra (b) and (c) which shows emission in UV as well as in the visible region. At λex_{338} only excitonic emission is observed at 380 nm. At λex_{275}, there are four peaks in emission spectrum at 304, 380, 423, and 488 nm. In both cases, peak at 380 nm is originated from excitonic recombination and consistent with the band-gap measurement of ZnO as shown in Figure 7. Other than excitonic peak, all other peaks in the visible region are considered to be from defects in literature.[55,56]

In our measurement, we do not expect emission to originate from interstitial vacancies or deep traps in the material, because the material characterization has shown very limited defects being present (e.g., see Raman spectrum in Figure 5, XPS analysis in Figure 6b and EDX in Figure 4b). However, there is visible emission at 423 nm and 488 nm at λex_{275} which shows little defects in the material. These emissions in the violet, blue region are considered to be because of structural defects, for example, oxygen vacancies, Zn interstitials, Zn vacancies, ionized charge states of intrinsic defects etc.[56] Another peak at 304 nm in UV region is also related to emission from zinc interstitials (Zn_i) to valence band transition as the position of Zn_i level is 0.22 eV below conduction band.[57] There is no emission related to defect states at near the band gap excitation wavelength.

Fermi level measurements were carried out using a scanning Kelvin probe (SKP 4.5, KP Technology Ltd. UK). The Fermi level was obtained by measuring the contact potential difference (CPD) between the ZnO sample and a reference electrode.

The calibration of the system was done by measuring the work function (ϕ) of a known gold reference. The Fermi level of the sample can then be calculated with

$$\phi_{\text{Sample}} = 5.1 - \text{CDP}_{\text{Au}} + \text{CDP}_{\text{Sample}} \quad (1)$$

where CPD_{Au} is the contact potential difference between the Au reference and Au tip, $\text{CPD}_{\text{Sample}}$ is the contact potential difference between sample and Au tip. This gives the Fermi level of the measured sample. In our case, the Fermi level of ZnO is −5.27 eV as can be seen in Figure 9. This value matches well with reported value of ZnO Fermi level (−5.2 eV).[58,59]

The complete band structure of ZnO has been drawn as shown in Figure 10. The position of the valence band edge

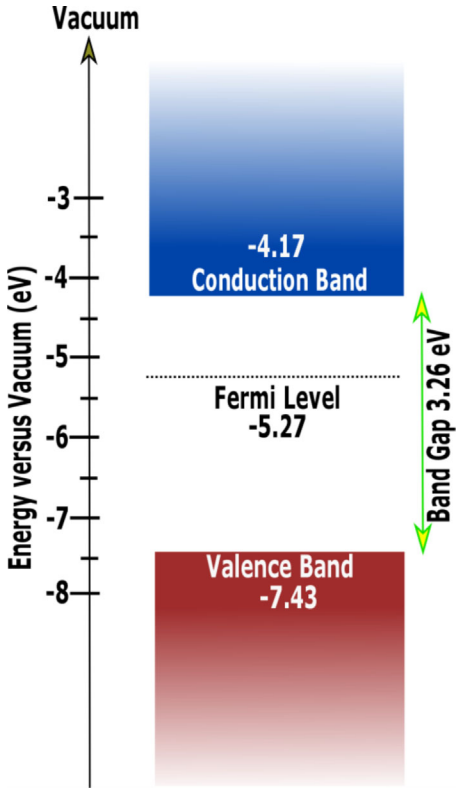

FIGURE 10 Estimated band diagram of ZnO

was calculated from the XPS results (E_f–E_{VBM} = 2.16 eV) and using the Fermi level value from Kelvin probe measurements, that is, $E_{VBM} = E_f$–2.16 eV = −5.27 −2.16 eV = −7.43 eV. The corresponding conduction band edge was also found adding the value of the measured bandgap energy to the valence band edge, yielding a value of −4.17 eV. The overall band structure is in good agreement with reported literature values.[59–61]

4 | CONCLUSION

Porous nanocrystalline ZnO films were synthesized and deposited by RF atmospheric pressure plasma in ambient conditions. Structural, chemical, and optical properties confirm the ZnO films to be stoichiometric with very low defect density. We have also carried out a complete experimental determination of the band energy diagram which confirms the film to preserve the required and desired energetics expected from ZnO films. This simple, low-cost and versatile synthesis method therefore shows the potential for direct deposition of porous ZnO films that can be implemented for a wide range of application where ZnO has been employed successfully.

ACKNOWLEDGMENTS

This work was supported by Engineering and Physical Sciences Research Council (EPSRC), grant EP/M024938/1 and EP/K022237/1.

REFERENCES

[1] T. Aoki, Y. Hatanaka, D. C. Look, *Appl. Phys. Lett*. **2000**, *76*, 3257.

[2] C. Y. Lee, Y. Y. Hui, W. F. Su, C. F. Lin, *Appl. Phys. Lett*. **2008**, *92*, 1.

[3] E. Neshataeva, T. Kümmell, G. Bacher, A. Ebbers, *Appl. Phys. Lett*. **2009**, *94*, 92.

[4] E. Nannen, T. Kümmell, A. Ebbers, G. Bacher, *Appl. Phys. Express* **2012**, *5*, 35001.

[5] T. Omata, Y. Tani, S. Kobayashi, K. Takahashi, A. Miyanaga, Y. Maeda, S. Otsuka-Yao-Matsuo, *Appl. Phys. Lett*. **2012**, *100*, 1.

[6] M. Law, L. E. Greene, J. C. Johnson, R. Saykally, P. Yang, *Nat. Mater*. **2005**, *4*, 455.

[7] G. B. E. Neshataeva, T. Kümmell, *Inorganic Nanoparticles: Synthesis, Applications, and Perspectives*. CRC Press, Taylor and Francis Group, United States **2011**.

[8] M. H. Huang, *Science (80-.)*. **2001**, *292*, 1897.

[9] N. Saito, H. Haneda, T. Sekiguchi, N. Ohashi, I. Sakaguchi, K. Koumoto, *Adv. Mater*. **2002**, *14*, 418.

[10] J. B. Cui, C. P. Daghlian, U. J. Gibson, R. Püsche, P. Geithner, L. Ley, *J. Appl. Phys*. **2005**, *97*, 044315.

[11] C. Ravichandran, J. Kumar, G. Srinivasan, C. Lennon, S. Sivananthan, *J. Mater. Sci. Mater. Electron*. **2015**, *26*, 5489.

[12] Z. Liu, Z. Jin, J. Qiu, X. Liu, W. Wu, W. Li, *Semicond. Sci. Technol*. **2005**, *21*, 60.

[13] B. Pal, M. Sharon, *Mater. Chem. Phys*. **2002**, *76*, 82.

[14] L. Wang, X. H. Zhang, K. Z. Chen, *CrystEngComm* **2013**, *15*, 4860.

[15] S. Sadofev, S. Blumstengel, J. Cui, J. Puls, S. Rogaschewski, P. Schäfer, Y. G. Sadofyev, F. Henneberger, *Appl. Phys. Lett*. **2005**, *87*, 31.

[16] Z. Yang, Z. Zuo, H. M. Zhou, W. P. Beyermann, J. L. Liu, *J. Cryst. Growth* **2011**, *314*, 97.

[17] S. Faÿ, L. Feitknecht, R. Schlüchter, U. Kroll, E. Vallat-Sauvain, A. Shah, *Sol. Energy Mater. Sol. Cells* **2006**, *90*, 2960.

[18] K. Haga, T. Suzuki, Y. Kashiwaba, H. Watanabe, B. P. Zhang, Y. Segawa, *Thin Solid Films* **2003**, *433*, 131.

[19] A. Illiberi, P. J. P. M. Simons, B. Kniknie, J. van Deelen, M. Theelen, M. Zeman, M. Tijssen, W. Zijlmans, H. L. A. H. Steijvers, D. Habets, A. C. Janssen, E. H. A. Beckers, *J. Cryst. Growth* **2012**, *347*, 56.

[20] X. Y. Z. H. Deng, J. J. Russell, R. N. Lamb, B. Jiang, Y. Lia, *Thin Solid Films* **2004**, *458*, 43.

[21] M. Ohyama, *J. Am. Ceram. Soc*. **1998**, *32*, 1622.

[22] Y. Li, L. Xu, X. Li, X. Shen, A. Wang, *Appl. Surf. Sci*. **2010**, *256*, 4543.

[23] C.-Y. Tsay, K.-S. Fan, S.-H. Chen, C.-H. Tsai, *J. Alloys Compd*. **2010**, *495*, 126.

[24] C.-Y. Tsay, C.-W. Wu, C.-M. Lei, F.-S. Chen, C.-K. Lin, *Thin Solid Films* **2010**, *519*, 1516.

[25] N. L. Tarwal, P. S. Patil, *Appl. Surf. Sci*. **2010**, *256*, 7451.

[26] P. M. R. Kumar, C. S. Kartha, K. P. Vijayakumar, *J. Appl. Phys*. **2005**, *98*, 023509.

[27] A. Chakraborty, T. Mondal, S. K. Bera, S. K. Sen, R. Ghosh, G. K. Paul, *Mater. Chem. Phys*. **2008**, *112*, 162.

[28] G. Adamopoulos, A. Bashir, W. P. Gillin, S. Georgakopoulos, M. Shkunov, M. A. Baklar, N. Stingelin, D. D. C. Bradley, T. D. Anthopoulos, *Adv. Funct. Mater*. **2011**, *21*, 525.

[29] N. L. Tarwal, V. V. Shinde, a. S. Kamble, P. R. Jadhav, D. S. Patil, V. B. Patil, P. S. Patil, *Appl. Surf. Sci* **2011**, *257*, 10789.

[30] R. Romero, D. Leinen, E. A. Dalchiele, J. R. Ramos-Barrado, F. Martín, *Thin Solid Films* **2006**, *515*, 1942.

[31] S. Rackauskas, K. Mustonen, T. Järvinen, M. Mattila, O. Klimova, H. Jiang, O. Tolochko, H. Lipsanen, E. I. Kauppinen, A. G. Nasibulin, *Nanotechnology* **2012**, *23*, 95502.

[32] X. Yan, X. Tong, J. Wang, C. Gong, M. Zhang, L. Liang, *Mater. Lett*. **2013**, *92*, 165.

[33] Y. Zhu, Y. Wang, G. Duan, H. Zhang, Y. Li, G. Liu, L. Xu, W. Cai, *Sensors Actuators, B Chem*. **2015**, *221*, 350.

[34] H. Chen, W. Li, Q. Hou, H. Liu, L. Zhu, *Electrochim. Acta* **2011**, *56*, 9459.

[35] K.-M. Chang, S.-H. Huang, C.-J. Wu, W.-L. Lin, W.-C. Chen, C.-W. Chi, J.-W. Lin, C.-C. Chang, *Thin Solid Films* **2011**, *519*, 5114.

[36] C. M. Hsu, H. C. Li, S. T. Lien, J. Z. Chen, I. C. Cheng, C. C. Hsu, *IEEE Trans. Plasma Sci*. **2015**, *43*, 670.

[37] C. M. Hsu, S. T. Lien, Y. J. Yang, J. Z. Chen, I. C. Cheng, C. C. Hsu, *Thin Solid Films* **2014**, *570*, 423.

[38] S. Stauss, Y. Imanishi, H. Miyazoe, K. Terashima, *J. Phys. D. Appl. Phys*. **2010**, *43*, 155203.

[39] H. C. Bajaj, A. B. Panda, A. Sinhamahapatra, A. K. Giri, P. Pal, S. K. Pahari, *J. Mater. Chem* **2012**, *22*, 17227.

[40] L. Wang, X. Zhang, K. Chen, *Cryst. Eng. Comm* **2013**, *15*, 4860.

[41] H.-J. Wang, Y.-Y. Sun, Y. Cao, X.-H. Yu, X.-M. Ji, L. Yang, *Chem. Eng. J*. **2011**, *178*, 8.

[42] J. Zhang, S. Wang, M. Xu, Y. Wang, B. Zhu, S. Zhang, W. Huang, S. Wu, *Cryst. Growth Des* **2009**, *9*, 3532.

[43] A. Becheri, M. Dürr, P. Lo Nostro, P. Baglioni, *J. Nanoparticle Res* **2008**, *10*, 679.

[44] M. H. Habibi, M. H. Rahmati, *Spectrochim. Acta—Part A Mol. Biomol. Spectrosc*. **2014**, *133*, 13.

[45] J. Singh, P. Kumar, K. S. Hui, K. N. Hui, K. Ramam, R. S. Tiwari, O. N. Srivastava, *CrystEngComm* **2012**, *14*, 5898.

[46] A. Šarić, S. Musić, M. Ivanda, *J. Mol. Struct*. **2011**, *993*, 219.

[47] L. Shi, K. Bao, J. Cao, Y. Qian, *CrystEngComm* **2009**, *11*, 2009.

[48] S. S. Lo, D. Huang, *Langmuir* **2010**, *26*, 6762.

[49] N. S. Ramgir, D. J. Late, A. B. Bhise, M. A. More, I. S. Mulla, D. S. Joag, K. Vijayamohanan, *J. Phys. Chem. B* **2006**, *110*, 18236.

[50] M. Wang, F. Ren, J. Zhou, G. Cai, L. Cai, Y. Hu, D. Wang, Y. Liu, L. Guo, S. Shen, *Sci. Rep*. **2015**, *5*, 12925.

[51] A. S. Alshammari, L. Chi, X. Chen, A. Bagabas, D. Kramer, A. Alromaeh, Z. Jiang, *RSC Adv*. **2015**, *5*, 27690.

[52] H. Wang, S. Baek, J. Song, J. Lee, S. Lim, *Nanotechnology* **2008**, *19*, 75607.

[53] V. P. Singh, C. Rath, *RSC Adv*. **2015**, *5*, 44390.

[54] N. S. Pesika, K. J. Stebe, P. C. Searson, *Adv. Mater*. **2003**, *15*, 1289.

[55] H.-M. Xiong, *J. Mater. Chem*. **2010**, *20*, 4251.

[56] D. Das, P. Mondal, *RSC Adv*. **2014**, *4*, 35735.

[57] V. Kumar, H. C. Swart, O. M. Ntwaeaborwa, R. E. Kroon, J. J. Terblans, S. K. K. Shaat, A. Yousif, M. M. Duvenhage, *Mater. Lett*. **2013**, *101*, 57.

[58] S. Ghosh, V. S. Goudar, K. G. Padmalekha, S. V. Bhat, S. S. Indi, H. N. Vasan, *RSC Adv*. **2012**, *2*, 930.

[59] K. K. a, X. W. Kyaw, J. L. Sun, J. X. Zhao, D. W. Wang, X. F. Zhao, X. W. Wei, H. Liu, V Demir, T. Wu, *J. Phys. D. Appl. Phys*. **2011**, *44*, 45102.

[60] X. Wang, C. J. Summers, Z. L. Wang, *Appl. Phys. Lett*. **2005**, *86*.

[61] X. Bai, E. G. Wang, P. Gao, Z. L. Wang, *Nano Lett*. **2003**, *3*, 1147.

How to cite this article: Jain G, Macias-Montero M, Velusamy T, Maguire P, Mariotti D. Porous zinc oxide nanocrystalline film deposition by atmospheric pressure plasma: Fabrication and energy band estimation. *Plasma Process Polym*. 2017;14: e1700052. https://doi.org/10.1002/ppap.201700052